



**AIAA-2001-0911**

**Reynolds Number Effects on a Supersonic  
Transport at Subsonic High-Lift Conditions  
(Invited)**

L. R. Owens, and R. A. Wahls  
NASA Langley Research Center  
Hampton, Virginia

**39th AIAA Aerospace Sciences Meeting & Exhibit**  
8-11 January 2001  
Reno, Nevada

# REYNOLDS NUMBER EFFECTS ON A SUPERSONIC TRANSPORT AT SUBSONIC HIGH-LIFT CONDITIONS

L. R. Owens\*, and R. A. Wahls†

Aerodynamics, Aerothermodynamics, and Acoustics Competency  
NASA Langley Research Center  
Hampton, Virginia

## **ABSTRACT**

A High Speed Civil Transport configuration was tested in the National Transonic Facility at the NASA Langley Research Center as part of NASA's High Speed Research Program. The primary purposes of the tests were to assess Reynolds number scale effects and high Reynolds number aerodynamic characteristics of a realistic, second generation supersonic transport while providing data for the assessment of computational methods. The tests included longitudinal and lateral/directional studies at transonic and low-speed, high-lift conditions across a range of Reynolds numbers from that available in conventional wind tunnels to near flight conditions. Results are presented which focus on Reynolds number and static aeroelastic sensitivities of longitudinal characteristics at Mach 0.30 for a configuration without an empennage. A fundamental change in flow-state occurred between Reynolds numbers of 30 to 40 million, which is characterized by significantly earlier inboard leading-edge separation at the high Reynolds numbers. Force and moment levels change but Reynolds number trends are consistent between the two states.

## **INTRODUCTION**

Ground to flight scaling remains one of many challenges facing today's designers of aerospace vehicles. The goal of ground to flight scaling is the preflight prediction of multiple key aerodynamic characteristics with sufficient accuracy to meet both performance guarantees and certification requirements. In other words, the designer and his company strive to know the performance of their vehicle with high confidence prior to flight, thus enabling optimal design trades prior to flight and elimination of costly fixes to the aircraft after the first flight. Specific challenges, experiences, and suggested approaches to ground to flight scaling have been documented extensively over the years for a variety of vehicle classes (refs. 1, 2, among many others). Reynolds number effects are foremost among many factors affecting successful ground to flight scaling (refs. 3 - 5). The Reynolds number is the ratio of inertial to viscous forces, and is the primary aerodynamic scaling parameter used to relate sub-scale wind tunnel models to full-scale aircraft in flight. The challenge of Reynolds number scaling increases with the size of a full-scale aircraft as the Reynolds number increment between that obtainable in conventional wind tunnels and flight conditions expands. Additionally, the challenge for both wind tunnel and computational approaches increases as flow features become dominated by viscous-sensitive phenomena such as boundary-layer transition, shock/boundary-layer interaction, and separation onset and progression.

The present investigation was conducted in support of NASA's High Speed Research (HSR) Program, Phase II, which was conducted from 1993-1999 (ref. 6). The objective of this program, which was NASA sponsored and jointly executed with US industry, was to develop critical high-risk

---

\* Aerospace Engineer, Subsonic Aerodynamics Branch, Senior Member, AIAA

† Assistant Head, Configuration Aerodynamics Branch, Associate Fellow, AIAA

airframe and propulsion technologies to enable industry development of an economically viable and environmentally acceptable second generation, high speed civil transport (HSCT). Aerodynamic performance, one of several broad airframe technology areas, included tasks to address Configuration Aerodynamics for high-speed conditions and High-Lift Technology for take-off and landing. These elements encompassed not only the challenge of efficient supersonic cruise flight, but also the off-design challenges (ref. 7) of efficient transonic cruise and acceleration and quiet high-performance take-off and landing. The objective of the High-Lift Technology task was the development of practical low-speed high-lift concepts and design and analysis methods to allow the HSCT to operate safely and efficiently and reduce terminal area noise. Towards this goal, a scaling effort was defined to reduce the risk in the design process by identifying those physical features of an actual flight vehicle that would contribute to the aerodynamic differences between it and wind-tunnel models of various scale. Figure 1 shows the nominal mission profile for the baseline reference configuration used in the HSR program, and comparison to the capability of several wind tunnels. The baseline reference configuration, known as Reference H, was provided by Boeing and represented a Mach 2.4, 300 passenger aircraft with a 5000 nautical mile range.

A series of wind tunnel tests was executed in the National Transonic Facility (NTF) at NASA Langley Research Center (LaRC) across a wide range of Reynolds numbers from that available in conventional wind tunnels to near flight condition at subsonic and transonic Mach numbers. The tests included longitudinal and lateral/directional studies with and without an empennage at transonic and low-speed, high-lift conditions. This paper presents results focused on the Reynolds number sensitivities of longitudinal characteristics at low-speed, high-lift conditions representative of take-off and landing for the configuration without the empennage; reference 8 provides similar results for transonic cruise conditions.

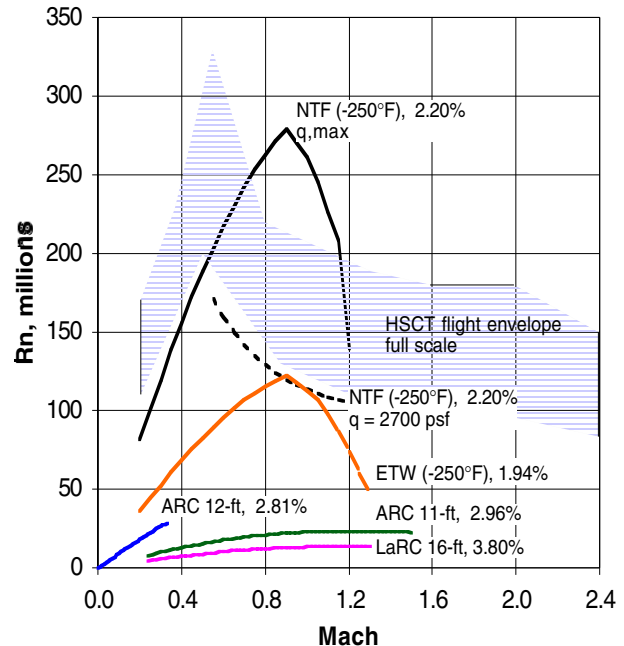


Figure 1. Nominal HSCT mission profile and wind tunnel capabilities (model scale adjusted to test section size, 2.2% scale in the NTF is the baseline size).

#### TERMS, ABBREVIATIONS, & ACRONYMS

|           |   |
|-----------|---|
| ARC       | NASA Ames Research Center                               |
| BL        | butt-line, model coordinates                            |
| $CI_{95}$ | 95% confidence interval                                 |
| $c$       | local chord length                                      |
| $C_D$     | drag coefficient  |
| $C_L$     | lift coefficient  |
| $C_M$     | pitching-moment coefficient referenced to $0.50mac$     |
| $C_p$     | pressure coefficient                                    |
| ETW       | European Transonic Windtunnel                           |
| FS        | fuselage station, model coordinates                     |
| HSCT      | High Speed Civil Transport                              |
| HSR       | High Speed Research                                     |
| LaRC      | Langley Research Center                                 |
| $M$       | Mach number   |
| $mac$     | mean aerodynamic chord                                  |
| NTF       | National Transonic Facility                             |
| $P_T$     | total pressure  |
| $q$       | dynamic pressure  |
| $Rn$      | Reynolds number based on $mac$                          |
| $r$       | local leading-edge radius                               |
| $T_T$     | total temperature                                       |
| $t_{max}$ | local maximum airfoil thickness                         |
| WL        | waterline, model coordinates                            |
| $\alpha$  | angle of attack   |
| $\eta$    | nondimensional semispan station                         |
| $\theta$  | sectional wing twist change, relative to wind-off twist |



Figure 2. External view of the NTF.

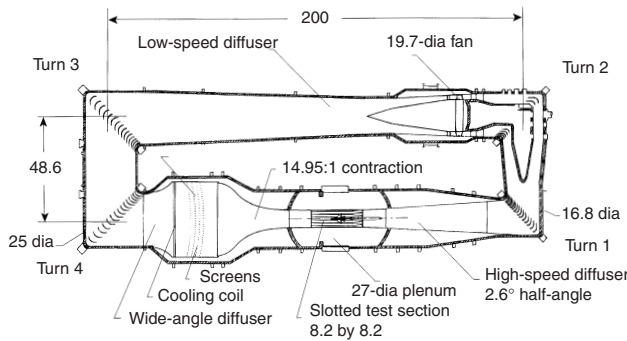


Figure 3. NTF circuit diagram (linear dimensions in ft).

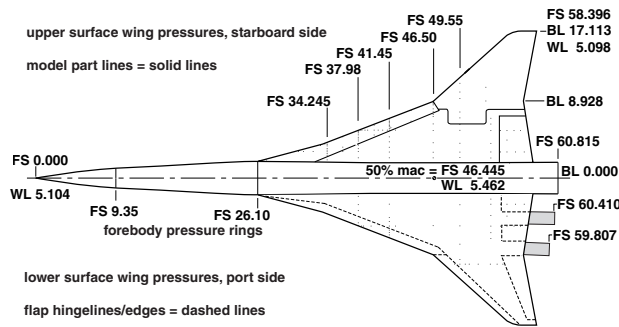


Figure 4. Model drawing with pressure locations (linear dimensions in inches).



Figure 5. 2.2% Reference H model in the NTF.

**EXPERIMENTAL APPROACH**

**Facility Description**

The NTF (ref. 9) is a unique national facility (fig. 2) that enables tests of aircraft configurations at conditions ranging from subsonic to low supersonic speeds at Reynolds numbers up to full-scale flight values, depending on the aircraft type and size. The facility (fig. 3) is a fan-driven, closed-circuit, continuous-flow, pressurized wind tunnel capable of operating in either dry air at warm temperatures or nitrogen from warm to cryogenic temperatures. The test section is 8.2 ft by 8.2 ft in cross section and 25 ft in length. The test section floor and ceiling are slotted (6 percent open), and the sidewalls are solid. Freestream turbulence is damped by four screens and a 14.95:1 contraction ratio from the settling chamber to the test section. Fan-noise effects are minimized by an acoustic treatment both upstream and downstream of the fan. A detailed assessment of the dynamic flow quality in the NTF is reported in reference 10, and reconfirmed with more recent measurements shown in reference 11. The NTF is capable of an absolute pressure range from 15 psi to 125 psi, a temperature range from  $-320^{\circ}\text{F}$  to  $150^{\circ}\text{F}$ , a Mach number range from 0.2 to 1.2, and a maximum Reynolds number of  $146 \times 10^6$  per ft at Mach 1. Typical tests use a temperature range from  $-250^{\circ}\text{F}$  to  $120^{\circ}\text{F}$ . Further facility details can be found in reference 12.

**Model Description**

The wind-tunnel model is a 2.2% scale representation of the HSR baseline configuration known as Reference H. Although the full model with empennage was tested during the HSR program, the present paper focuses on results obtained for the wing/body configuration with the body truncated slightly aft of the wing trailing edge. Figure 4 shows a planform drawing of the model with wing pressure taps and reference locations noted. The model has a cranked-delta wing planform with an aspect ratio of 2.367, a span of 34.23 inches, and a mean aerodynamic chord of 22.71 inches. The inboard wing ( $\eta \leq 0.522$ ) has a blunt ( $r/c \sim 0.0025$  to  $0.0030$ ) subsonic leading-edge with a sweep change from 76 to 68.5 deg at  $\eta = 0.226$ , a twist varying from approximately 1 deg near  $\eta = 0.10$  to  $-2$  deg near  $\eta = 0.50$ , and variable thickness ratio ( $t_{\text{max}}/c$ ) from 0.043 to 0.024. The outboard, supersonic leading edge is sharp, swept 48 deg, has a constant twist of  $-1.6$  deg for  $\eta \geq 0.65$ , and a constant thickness ratio of

|  |        |
|--|--------|
| ref. area / NTF cross sectional area   | 0.0515 |
| model span / NTF width                 | 0.3478 |
| solid blockage ratio, $\alpha = 0$ deg | 0.0022 |

**Table 1. Model size relative to the NTF test section.**

0.024. The reference area for the model is 3.436 ft<sup>2</sup>. Table 1 provides several key ratios relating the model size to the NTF test section.

The model was designed and constructed specifically for testing in the cryogenic, pressurized conditions of the NTF, where dynamic pressures reached approximately 2700 psf during these tests at transonic conditions; the model jig shape was that of the Mach 2.4 cruise design point. The model was built of maraging steel with a surface finish of 8-16 $\mu$ -inches (root mean square) and a contour tolerance of  $\pm 0.005$  inches. The model is shown in figure 5 mounted in the NTF test section on a straight sting; the sting mounts to a 6-deg offset stub sting which in turn mounts to the facility arcsector resulting in a model angle-of-attack range from  $-4$  to 24 degrees.

The model has multiple inboard leading and trailing edge parts, multiple outboard wing panels each with different leading and trailing edge deflections, and four detachable, 8.43 inch long, constant internal diameter (1.236 inches), circular flow-through nacelles with boundary-layer diverters located between the wing and nacelle. The inboard nacelles are rigged with toe-in and pitch (nose down) angles of 1 and 4.17 deg, respectively; the outboard nacelles are rigged with toe-in and pitch angles of 2.4 and 2.84 deg, respectively. The multiple leading and trailing edge parts in combination with the multiple outboard panels enabled testing of a variety of configurations including the baseline (supersonic cruise), take-off, landing, stall recovery, and transonic cruise configurations as defined in table 2. Results for the baseline and take-off configurations (with the nacelle/diverters) are included herein.

The model was instrumented with 48 forebody pressures distributed circumferentially at two fuselage stations and 146 wing pressures distributed in both spanwise and chordwise rows on the starboard upper and port lower surfaces of the wing, as shown in figure 4. Additionally, one inboard and one outboard nacelle were instrumented with an internal Preston tube, and 6 nacelle base pressure taps enabling correction for nacelle internal and base drag effects.

**Instrumentation**

Aerodynamic force and moment data were obtained with an internal, unheated, six-component, strain gauge balance. The balance used was one of the NTF-113-class balances having the load capacity and accuracy shown in table 3. An internal, heated accelerometer package was used to measure the onboard angle

| Designation      | LE Deflection, deg<br>Inboard/Outboard | TE Deflection, deg<br>Inboard/Outboard |
|------------------|--|--|
| Baseline         | 0/0                                    | 0/0                                    |
| Take-Off         | 30/30                                  | 10/10                                  |
| Landing          | 30/30                                  | 20/20                                  |
| Stall Recovery   | 50/50                                  | 30/30                                  |
| Transonic Cruise | 0/10                                   | 0/3                                    |

**Table 2. Available Wing Configurations.**

| Component     | Full-Scale Load | Nominal Accuracy<br>95% confidence |
|---------------|-----------------|------------------------------------|
| Normal, lbs   | $\pm 6500$      | $\pm 0.09\%$ full-scale            |
| Axial, lbs    | $\pm 400$       | $\pm 0.30\%$ full-scale            |
| Side, lbs     | $\pm 4000$      | $\pm 0.18\%$ full-scale            |
| Pitch, in-lbs | $\pm 13000$     | $\pm 0.09\%$ full-scale            |
| Yaw, in-lbs   | $\pm 6500$      | $\pm 0.18\%$ full-scale            |
| Roll, in-lbs  | $\pm 9000$      | $\pm 0.29\%$ full-scale            |

**Table 3. NTF-113 balance capacity and accuracy.**

of attack; quoted accuracy of the package under smooth operating wind tunnel conditions is  $\pm 0.01$  deg (ref. 13). Model pressure measurements were obtained using three 48-port, 30-psid, onboard, heated, electronically scanned pressure (ESP) transducers with a quoted accuracy of  $\pm 0.2\%$  of full-scale (worst case) throughout the range. The body cavity pressure was measured with a heated, 5-psid ESP module located in the facility arcsector. Wing deformation measurements were made at 3 spanwise stations,  $\eta = 0.635, 0.778, \text{ and } 0.922$ , using a video model deformation system (ref. 14). The system provided sectional twist change data relative to the wind-off shape with a quoted accuracy of  $\pm 0.10$  deg.

The primary measured flow variables include both the total and static pressures and the total temperature. Mach number, Reynolds number, and dynamic pressure are calculated from these measured parameters. A complete

description of these measurements and subsequent calculations is given in reference 15.

### Data Reduction and Corrections

Information on the various instrumentation devices, the data acquisition and control computers, and the data reduction algorithms for the different measurement systems is provided in reference 15. Standard balance, angle-of-attack, and tunnel parameter corrections have been applied. Note that the use of unheated balances in the cryogenic environment requires additional attention towards temperature compensation. The temperature compensation methods are designed to correct balance output due to thermal loads (refs. 15,16). Body cavity pressure and nacelle internal drag and base pressure corrections were applied based on the measurements described previously. The angle of attack was corrected for flow angularity (upflow) by measurement of both upright and inverted model force data for a given configuration and flow condition. Wall and model support interference effects have not been accounted for in the data; these effects were minimized through model sizing (table 1).

### Test Conditions

The NTF allows testing across a wide range of Reynolds numbers from that available in conventional wind tunnels to near flight conditions at subsonic and transonic Mach numbers. Tests of the 2.2% Reference H model spanned Mach numbers from 0.30 to 1.10, and Reynolds numbers from 4 to 120 million based on the mean aerodynamic chord. The present paper focuses on the low-speed regime representative of take-off and landing, and specifically at Mach 0.30 for a Reynolds number range from 8.5 to 90 million. Figure 1 indicates the relationship of the NTF test conditions to flight, and figure 6 provides the NTF operational envelope for Mach 0.30 with specific test points identified. Full-scale flight Reynolds numbers were not obtainable due to the large size of the full-scale aircraft and model size and load limitations ( $q = 2700$  psf boundary in figure 1) at least in part driven by the requirement of testing the same model at transonic conditions.

The goals of assessing Reynolds number scale effects and extrapolation to flight conditions required a series of intermediate conditions to better identify trends. As seen in figure 6, the desired Reynolds number range could not be covered at a constant total pressure level, and

thus dynamic pressure level. However, the independent control of total pressure, total temperature, and fan speed in the NTF allow the isolation of pure Reynolds effects, pure static aeroelastic (dynamic pressure) effects, and pure compressibility (Mach) effects. Several conditions are used to isolate static aeroelastic effects from the Reynolds number effects for Mach 0.30 as shown in figure 6. During Reynolds number sweeps, it is actually the ratio of dynamic pressure ( $q$ ) to the model material modulus of elasticity ( $E$ ) that is held constant to maintain a constant static aeroelastic state ( $q/E$ ) due to the variability of the modulus of elasticity over the temperature range of the NTF. Note that constant  $q/E$  was not maintained for the two lowest Reynolds number

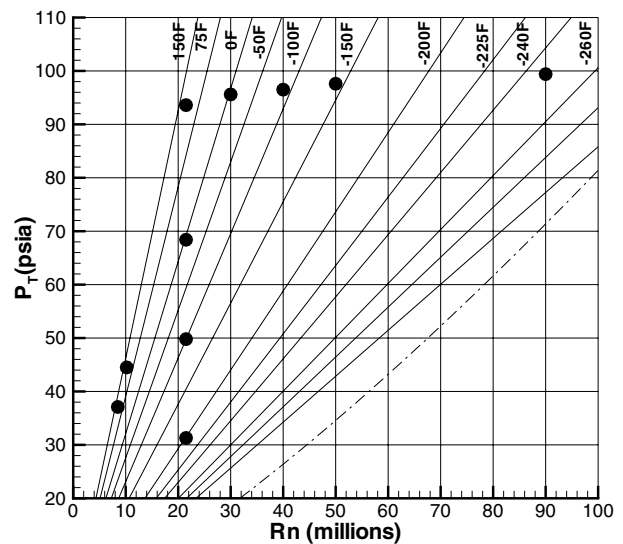


Figure 6. NTF operational envelope, Mach =0.30.

conditions due to the use of air rather than nitrogen to conserve resources. However, the aeroelastic adjustment methodology (explained in Results & Discussion section) is sufficient to provide pure Reynolds number effects at this lower dynamic pressure level.

### Boundary-Layer Transition

A basic strategy used in the NTF includes testing at high Reynolds number conditions with free transition. The high Reynolds number test condition typically corresponds to a design flight condition. To anchor the NTF data to low Reynolds number data obtained in a conventional wind tunnel, the NTF model is usually tested at a matching low Reynolds number condition with the boundary-layer tripping (forced transition) strategy

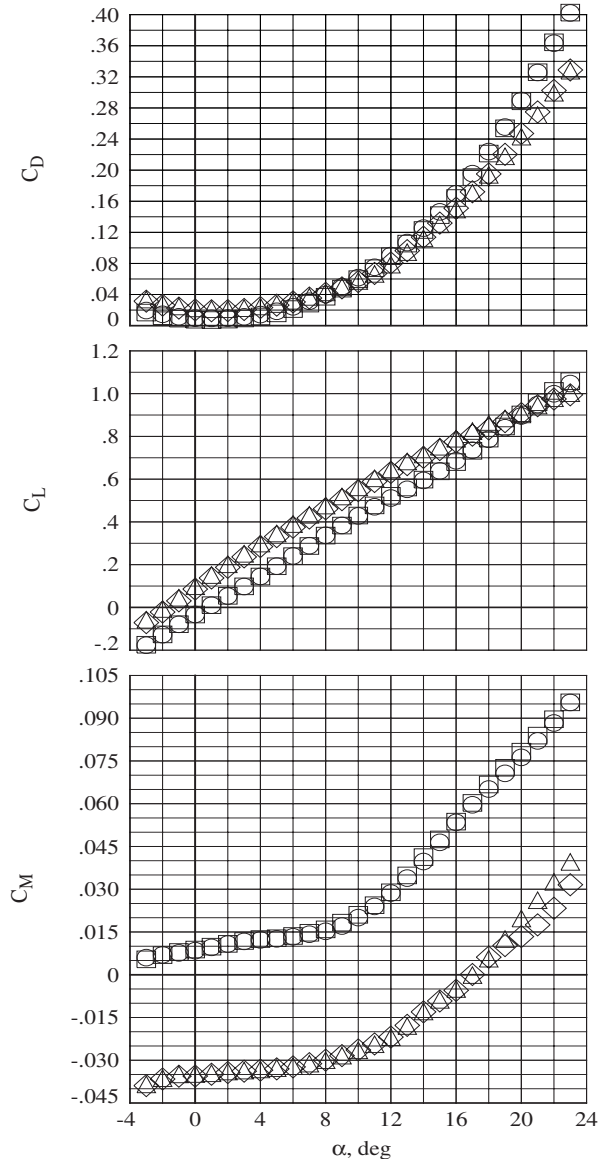
used in that facility. The majority of the data for the 2.2% Reference H model was not acquired with fixed transition on the wing, primarily due to the potential at the time for a one-third-scale flight test (which never occurred) anticipated to fly at conditions susceptible to transitional flow. No data with fixed transition on the wing is available for configurations presented herein. Transition was consistently fixed on the forebody with a ring of carborundum grit located 1.5 inches from the nose, and on the nacelle internal surface to facilitate the internal nacelle drag correction. These trips were sized and located based on traditional criteria (ref. 17).

**RESULTS & DISCUSSION**

The purpose of this paper is to document the Reynolds number sensitivities of longitudinal aerodynamic characteristics for a relevant, supersonic transport configuration at conditions representative of take-off and landing, Mach 0.30. Though the configuration was tested with an empennage, the present results are limited to the wing/body configuration with installed nacelles. Figure 7 presents representative data for the baseline and take-off configurations at Reynolds numbers of 8.5 and 90 million, and is provided to indicate the basic, longitudinal aerodynamic characteristics of the configuration. The data as acquired, and presented in figure 7, include the combined effects of static aeroelastic deformation and Reynolds number effects; this fact is highlighted in figure 7 by the distinctly different dynamic pressure levels for the two Reynolds numbers. The discussion will address static aeroelastic effects as a means to isolate and more properly address Reynolds number effects.

**Repeatability**

Data presented herein were acquired within a single wind-tunnel test of the model. This section provides examples of short-term repeatability (within test / Mach series), as defined in reference 18, quantified in terms of a 95% confidence interval for each configuration. The 95% confidence interval is interpreted as the bounds about an estimated mean (average of multiple, repeat polars) that encompasses the true mean value with a chance of 95%. Examples of short-term repeatability of longitudinal aerodynamic data are shown in figure 8 for the baseline and take-off configurations at a Reynolds number of 90 million. The figure shows the



|   | Rn (millions) | q, psf | config         |
|---|---------------|--------|----------------|
| ○ | 8.51          | 318.   | Baseline + nac |
| □ | 90.00         | 839.   | Baseline + nac |
| ◇ | 8.52          | 318.   | Take-off + nac |
| △ | 89.95         | 842.   | Take-off + nac |

**Figure 7. Representative longitudinal force and moment data, M = 0.30.**

residuals of the longitudinal coefficients defined as the difference in the individual measured data points from the estimated mean of the group of repeated polars; the estimated mean was the average of the grouped data based on piecewise, 2<sup>nd</sup> order polynomial fits of the individual polars. The figure also indicates, with a solid line, the

bounds of the 95% confidence interval as a function of angle of attack; the average confidence interval over the range of angle of attack is noted.

Results shown in figure 8 are typical of other test conditions. In general, the coefficient residuals are small up to angles-of-attack of approximately 12 deg. Beyond this angle of attack range, larger-scale separations begin to dominate the wing flow field as indicated by the more nonlinear behavior exhibited in the pitching moment coefficient data and the increasing variations in the drag residual data. For reference, the average 95% confidence interval values for each coefficient at each test condition are included in table 4. These values were used to determine the significance of the differences observed in the data.

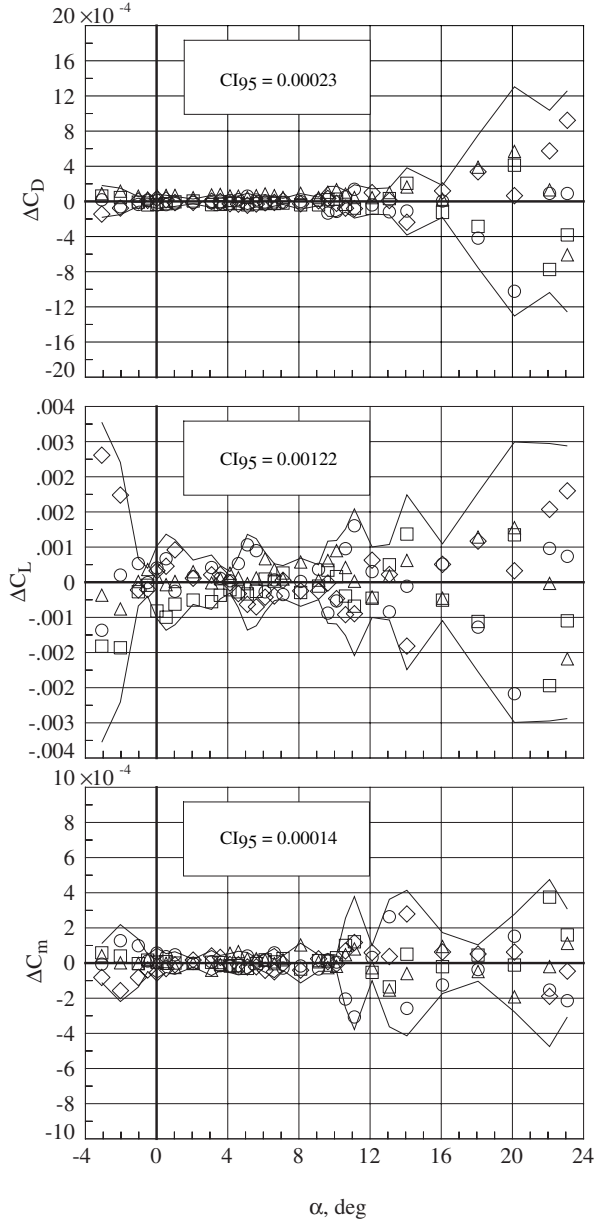
| Rn   | q, psf | $\Delta C_D$ | $\Delta C_L$ | $\Delta C_M$ |
|------|--------|--------------|--------------|--------------|
| 8.5  | 318    | 0.00011      | 0.00050      | 0.00007      |
| 10.2 | 381    | 0.00010      | 0.00047      | 0.00007      |
| 21.6 | 267    | 0.00028      | 0.00092      | 0.00015      |
| 21.6 | 430    | 0.00027      | 0.00096      | 0.00019      |
| 21.6 | 587    | 0.00007      | 0.00037      | 0.00006      |
| 21.6 | 803    | 0.00012      | 0.00065      | 0.00008      |
| 30.0 | 817    | 0.00011      | 0.00076      | 0.00011      |
| 40.0 | 825    | 0.00047      | 0.00136      | 0.00190      |
| 50.0 | 834    | 0.00027      | 0.00113      | 0.00140      |
| 90.0 | 839    | 0.00023      | 0.00122      | 0.00140      |

a) Baseline configuration.

| Rn   | q, psf | $\Delta C_D$ | $\Delta C_L$ | $\Delta C_M$ |
|------|--------|--------------|--------------|--------------|
| 8.5  | 318    | 0.00012      | 0.00059      | 0.00009      |
| 10.2 | 381    | 0.00013      | 0.00051      | 0.00010      |
| 21.6 | 267    | 0.00019      | 0.00064      | 0.00013      |
| 21.6 | 430    | 0.00040      | 0.00134      | 0.00029      |
| 21.6 | 587    | 0.00010      | 0.00037      | 0.00005      |
| 21.6 | 803    | 0.00018      | 0.00100      | 0.00014      |
| 30.0 | 817    | 0.00018      | 0.00074      | 0.00008      |
| 40.0 | 825    | 0.00029      | 0.00062      | 0.00015      |
| 50.0 | 834    | 0.00022      | 0.00066      | 0.00009      |
| 90.0 | 839    | 0.00030      | 0.00133      | 0.00017      |

b) Take-Off configuration.

Table 4. Repeatability data (95% confidence intervals averaged over  $\alpha$  range).

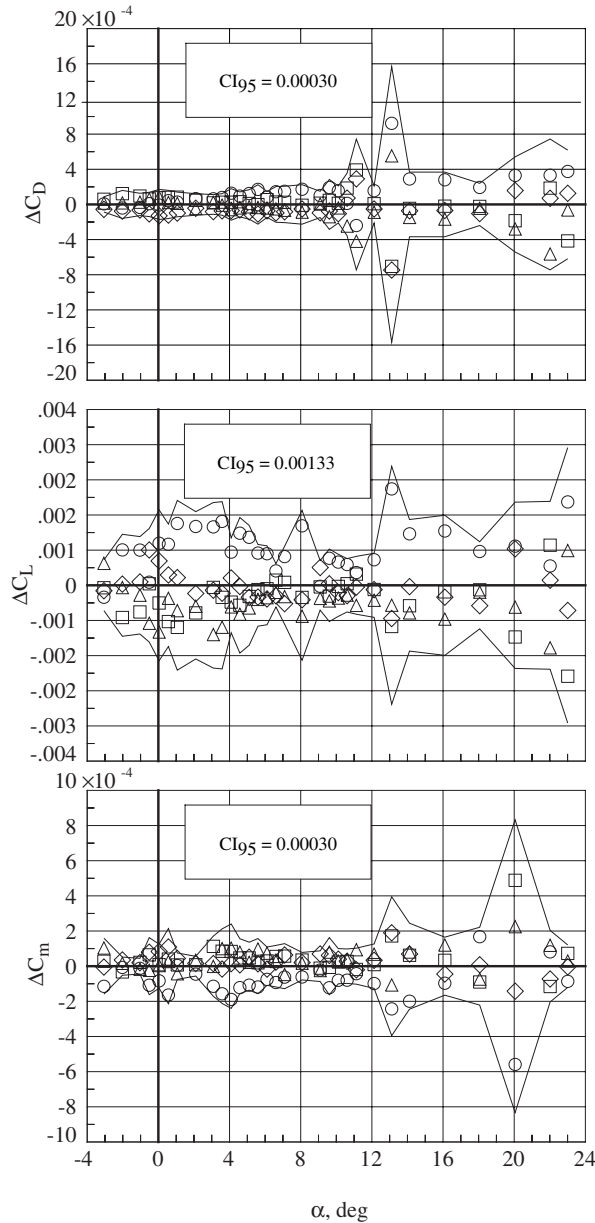


Rn (millions) P<sub>T</sub>, psi T<sub>T</sub>, °F q, psf

- 90.05 99.41 -247.5 839.2
- 90.02 99.41 -247.4 839.6
- ◇ 89.99 99.41 -247.4 839.1
- △ 89.95 99.40 -247.3 839.5

a) Baseline configuration with nacelles.

Figure 8. Short-term repeatability, M = 0.30.



|   | Rn (millions) | P <sub>T</sub> , psi | T <sub>T</sub> , °F | q, psf |
|---|---------------|----------------------|---------------------|--------|
| ○ | 90.06         | 99.40                | -247.2              | 842.2  |
| □ | 89.80         | 99.40                | -247.0              | 840.2  |
| ◇ | 89.92         | 99.40                | -247.2              | 840.5  |
| △ | 90.03         | 99.40                | -247.1              | 843.1  |

b) Take-off configuration with nacelles.

Figure 8. Concluded.

The wing pressure data presented in this report did not have repeat run sets available to evaluate the repeatability of this data. However, the consistency of the pressure coefficients at the lower angles of attack as well as the repeatability during the aeroelastic sweeps provided some confidence that differences of the order of 0.1 were distinguishable.

**Static Aeroelastic Effects**

Achieving high Reynolds numbers approaching those characteristic of flight requires the manipulation of both the total temperature and pressure, as seen in figure 6. As a result, the static aeroelastic deformation of the model, in particular the wing, under load must be considered when attempting to isolate Reynolds number effects. Previous reports for high aspect ratio subsonic transport configurations have shown the static aeroelastic effects to be on the order of Reynolds number effects, and often opposite in sense to that of Reynolds number trends, thus masking the Reynolds number effects (ref. 19, 20). Like the subsonic transport configurations, the current low aspect ratio HSCT model is flexible under load, most notably on the thin outboard wing panel.

Video model deformation measurements of the wing under load were concentrated on the outboard wing panel. These measurements indicated that as the aerodynamic load on the wing increased, the outboard wing panel would tend to washout, similar to that observed on the higher aspect ratio subsonic transports. This type of wing bending occurs because the local lifting center of pressure is located behind the elastic axis of the wing, which produces a local nose-down torsional moment at each outboard wing section. Figure 9 shows representative wing twist data at η = 0.922, relative to the wind-off twist, as a function of dynamic pressure and angle of attack. At the higher dynamic pressures and/or higher angles of attack, the local twist change increases (more nose-down) on the order of 1 deg. The relationship between local wing twist change and dynamic pressure is linear, at least over the range of dynamic pressure shown here. One would expect that extrapolation to the wind-off condition (q = 0 psf) would indicate no twist change; the data at α = 9 deg does approach this result for the baseline wing configuration.

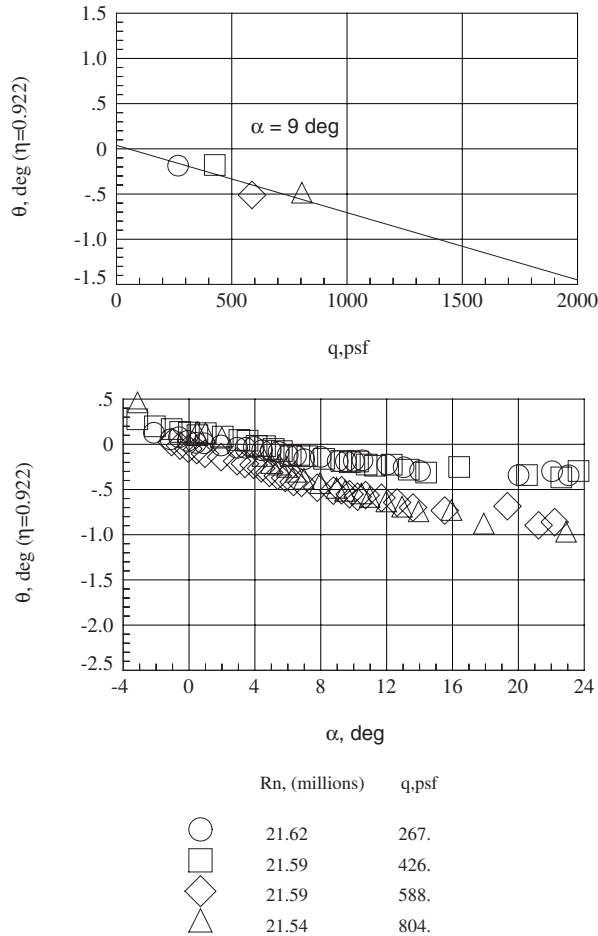
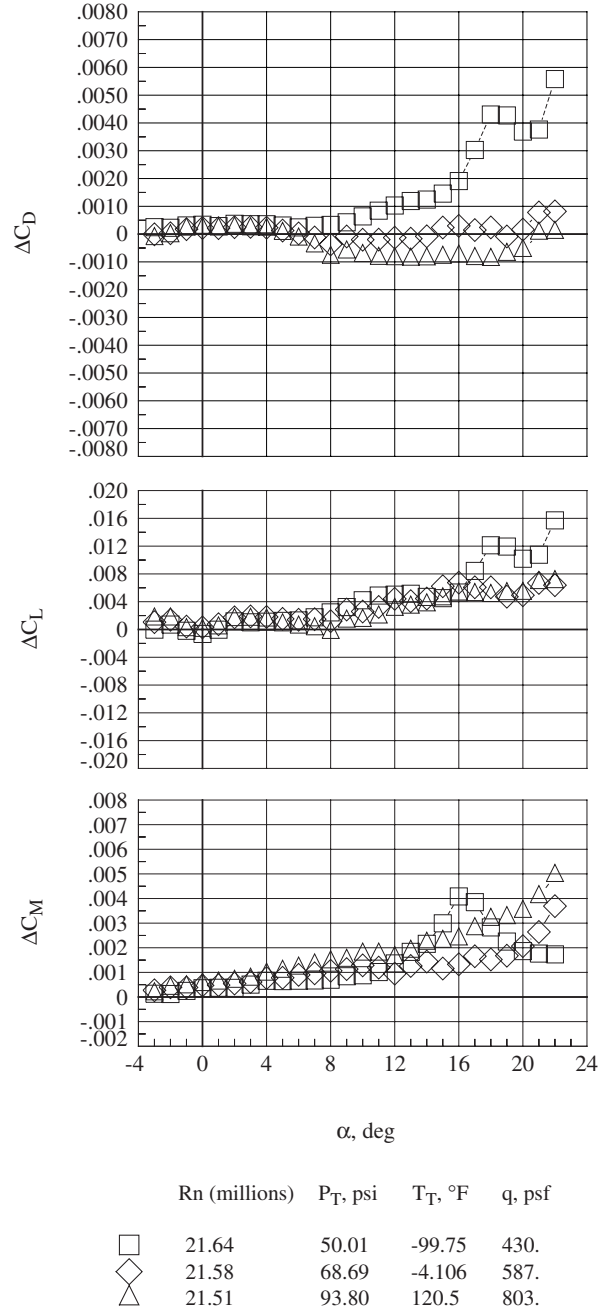


Figure 9. Outboard wing twist change under load, baseline configuration with nacelles, M = 0.30.

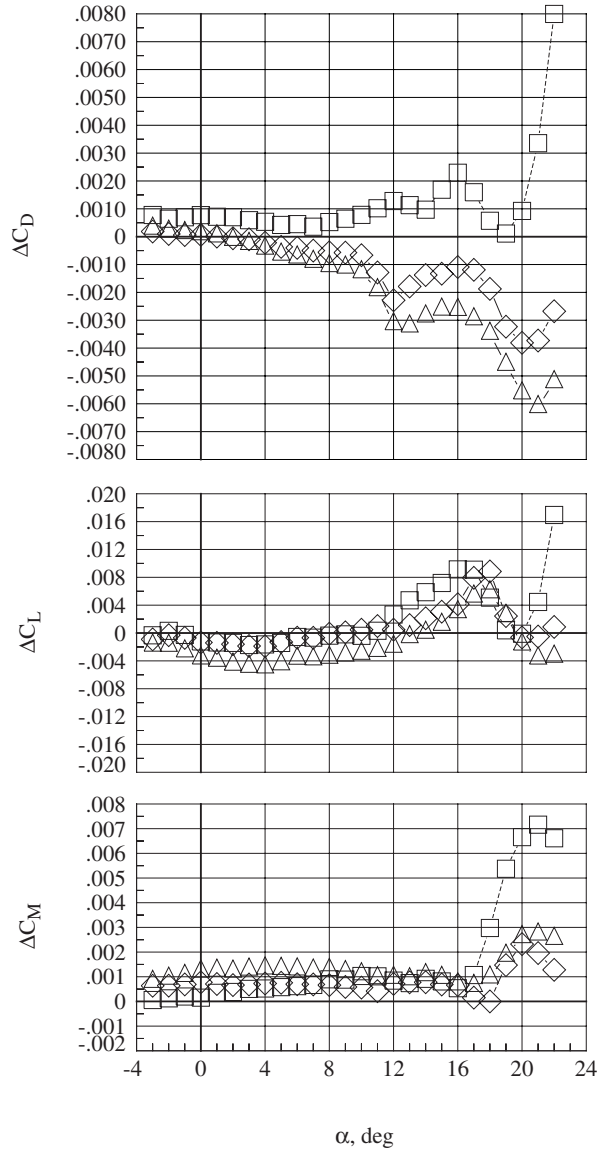
The effects of static aeroelastic wing bending on the longitudinal aerodynamic data obtained are presented in figure 10. These data were obtained with a constant Reynolds number of 21.6 million for several total pressure (dynamic pressure) conditions, as shown in figure 6. The data for the dynamic pressure level of about 430 psf is significantly different from the other three dynamic pressure levels surrounding it, especially the drag increments for both configurations. This difference was also observed in the wing pressure data for the baseline configuration. An example of two pressures near the wing leading edge as a function of angle of attack is shown in figure 11. The inboard wing pressure ( $\eta = 0.405$ ) data for the dynamic pressure level of about 430 psf show a much earlier leading-edge separation than that of the other three dynamic pressures that surround it. This suggests that it is likely there was something other than model deformation affecting the 430 psf data. The outboard wing pressure ( $\eta = 0.619$ ) also



a) Baseline configuration with nacelles.

Figure 10. Static aeroelastic effects on longitudinal coefficients, reference to q = 267 psf, M = 0.30.

show a slight difference in the 430 psf data from that of the other three dynamic pressure levels. The cause for this difference was not clear (and remains unclear) from the available data. One possible explanation for the difference at the 430 psf test conditions is that unobservable frost may have developed on the wing leading edge

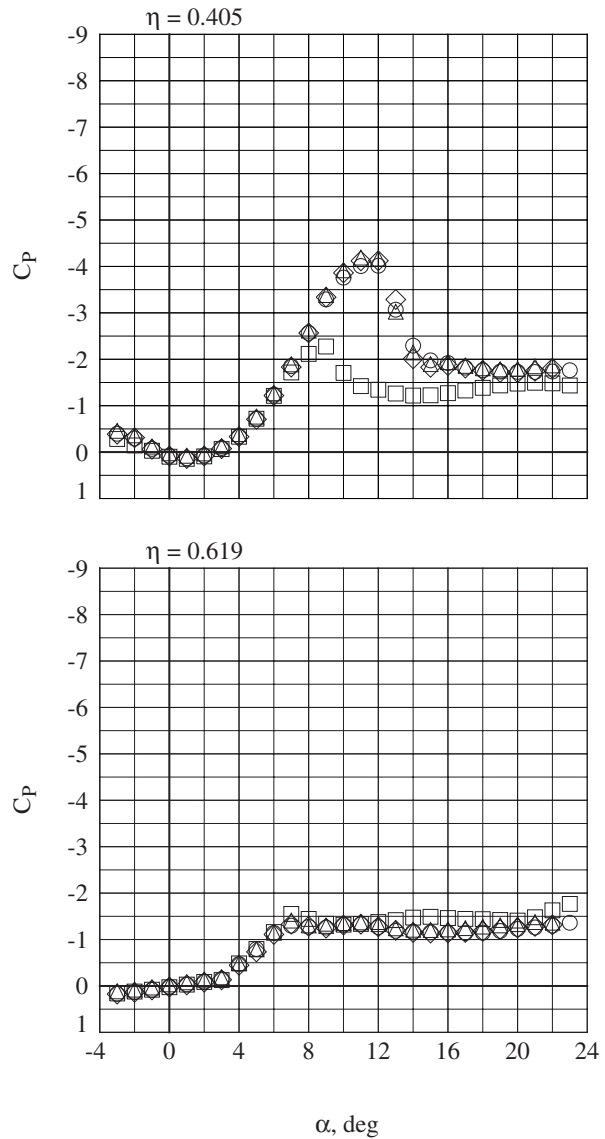


|   | Rn (millions) | P <sub>T</sub> , psi | T <sub>T</sub> , °F | q, psf |
|---|---------------|----------------------|---------------------|--------|
| □ | 21.60         | 50.01                | -100.2              | 427.   |
| ◇ | 21.59         | 68.71                | -3.991              | 588.   |
| △ | 21.55         | 93.82                | 120.5               | 806.   |

b) Take-off configuration with nacelles.

Figure 10. Concluded.

and influenced the separation characteristics. Recent testing of a subsonic transport semi-span model, documented in reference 21, indicates that tunnel test conditions below the dewpoint for the test gas sometimes produced frost on the model, especially in regions of highly accelerated flow. However, there were no reports of frost observed on the model during the HSR test. Also, measurements of losses in the tunnel circuit (i.e.,



|   | Rn (millions) | q, psf | T <sub>T</sub> , °F |
|---|---------------|--------|---------------------|
| ○ | 21.62         | 267.   | -201.9              |
| □ | 21.59         | 426.   | -100.1              |
| ◇ | 21.59         | 588.   | -4.028              |
| △ | 21.55         | 804.   | 120.0               |

Figure 11. Wing leading-edge pressure characteristics, baseline configuration with nacelles, M = 0.30.

at the cooling coil), which tend to increase as frost accumulates, were not consistent enough to conclude that frost was a factor for this data. Another possible cause is that the flow field is very sensitive to transitional flow at this intermediate Reynolds number, and causes changes in boundary-layer state.

When the anomalous 430 psf data runs are ignored in figure 10, the force and moment

increments tend to behave in a consistent manner as dynamic pressure and angle of attack increase for both configurations shown. The drag change for both configurations tends to decrease with increasing dynamic pressure at the higher angles of attack. The sensitivity to dynamic pressure change increased up to a certain angle of attack, about 8 deg for the baseline and about 12 deg for the take-off configuration, and then became nearly constant. This behavior suggested that the outboard wing loads increased the washout up to these angles of attack and then did not produce any further twisting as the model attitude increased. The washout tendency is also supported by the twist data for the baseline configuration, which generally showed that the twist changed less as the angle of attack increased beyond an angle of attack of about 8 deg (see figure 9). No wing twist measurements were made for the take-off configuration, but the character of the drag changes is consistent with a washout tendency similar to that observed for the baseline configuration.

The lift change for the baseline configuration was relatively insensitive to dynamic pressure changes up to an angle of attack of about 8 deg. Beyond this angle of attack, the lift increased with increasing dynamic pressure. This lift increase occurred in the same angle of attack region where the wing washout was relatively constant. The lift change for the take-off configuration was more sensitive to dynamic pressure changes than for the baseline configuration because the outboard wing panel is more highly loaded with the deflected flaps. Up to an angle of attack of about 12 deg, the lift decreased with increasing dynamic pressure for the take-off configuration, which was consistent with the expected increase in washout with increased dynamic pressure. Above this angle of attack, the lift increased with increasing dynamic pressure in the angle of attack region where it is expected that the washout has become constant. This behavior is similar to that observed for the baseline configuration.

The pitching moment change for the baseline configuration showed an increased sensitivity to dynamic pressure as the angle of attack increased. As the dynamic pressure increased, the baseline configuration generated a nose up moment change over the entire angle-of-attack range. The take-off configuration also generated a nose-up moment increment over the

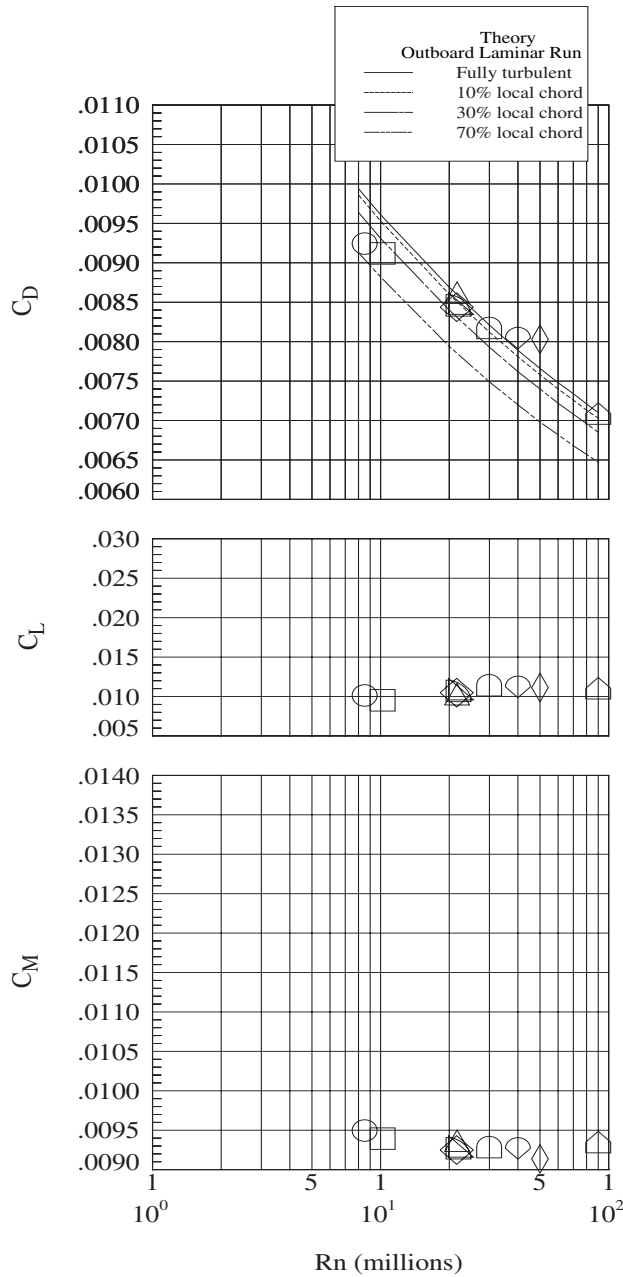
angle-of-attack range with increased dynamic pressure. However, the sensitivity to dynamic pressure was relatively constant over most of the angle-of-attack range.

At this point in the analysis, the difference in the data at the 430 psf (nominal) dynamic pressure level was deemed due to something other than static aeroelastic effects. As a result, static aeroelastic adjustments to the longitudinal force and moment coefficients were based on the sensitivities derived from the three nominal levels of 270, 590 and 800 psf for each configuration. These adjustments are applied to essentially account for static aeroelastic effects when isolating pure Reynolds number effects; in general, data was translated to the 270 psf dynamic pressure level when isolating Reynolds number effects.

### **Reynolds Number Effects**

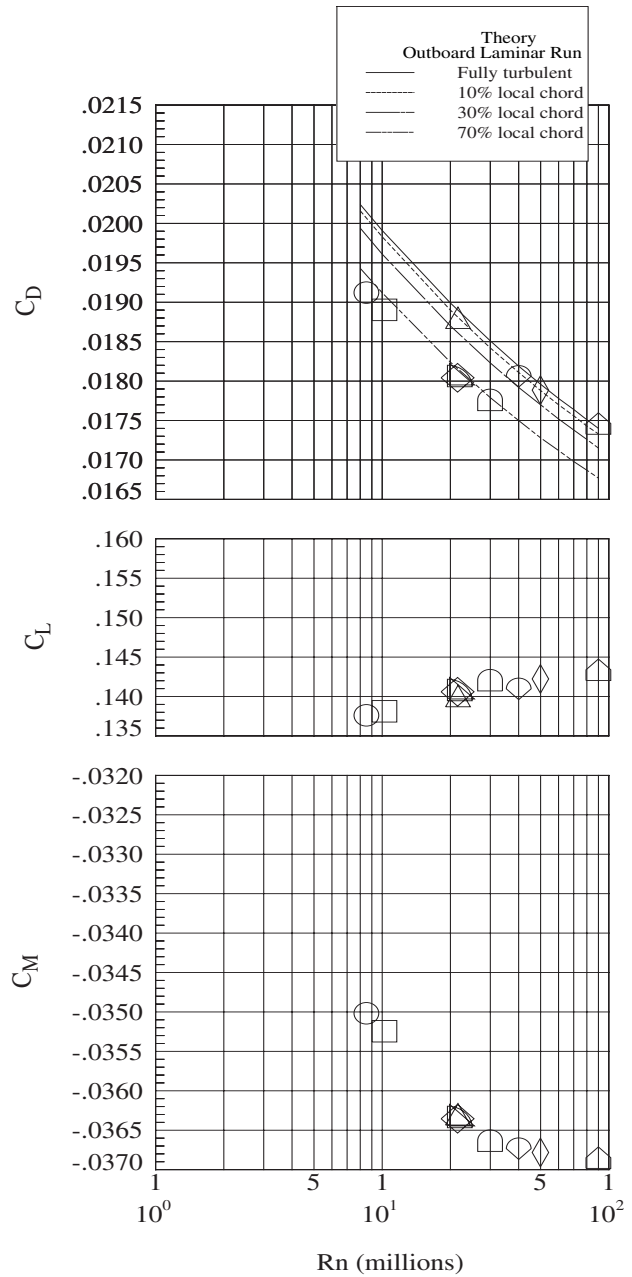
The primary Reynolds number effects observed in the data were a drag reduction and delay of leading-edge flow separation. A fundamental change of flow-state occurs between Reynolds numbers of 30 and 40 million, which is characterized by significantly earlier inboard leading--edge separation at the high Reynolds numbers. The following discussion will examine the Reynolds number trends for the longitudinal force and moment coefficients (adjusted for static aeroelastic effects) at two angles of attack. These angles of attack are characterized as follows: 1) near minimum drag ( $\alpha = 1$  deg), and 2) near the take-off design condition ( $\alpha = 9$  deg). Force and moment data for the baseline and take-off configurations, both with nacelles installed, are presented for each of these angles of attack.

The Reynolds number effects for conditions near minimum drag are presented in figure 12 for each configuration. Drag decreases as the Reynolds number increases, and is mostly accounted for by the established trend of skin friction with Reynolds number. Theoretical skin friction drag for the configuration was calculated using equivalent flat plate theory, plus form factors, using the Blasius and Karman-Schoenherr incompressible skin friction correlations for laminar and turbulent boundary layers, respectively, with compressibility effects accounted for with the reference temperature method (ref. 22). As applied herein, the flat-plate theory assumed that the same extent of laminar flow was present on both the upper and lower outboard wing surfaces



|   | $\alpha$ , deg | Rn (millions) | q, psf | $P_T$ , psi | $T_T$ , °F |
|---|----------------|---------------|--------|-------------|------------|
| ○ | 1.0            | 8.51          | 318.   | 37.12       | 120.6      |
| □ | 1.0            | 10.20         | 381.   | 44.52       | 120.3      |
| ◇ | 1.0            | 21.55         | 267.   | 31.32       | -201.5     |
| △ | 1.0            | 21.64         | 430.   | 50.01       | -99.75     |
| ▽ | 1.0            | 21.58         | 587.   | 68.69       | -4.106     |
| ◊ | 1.0            | 21.51         | 803.   | 93.80       | 120.5      |
| ◐ | 1.0            | 29.91         | 817.   | 95.30       | -4.090     |
| ◑ | 1.0            | 40.00         | 825.   | 96.41       | -90.38     |
| ◒ | 1.0            | 49.97         | 834.   | 97.20       | -143.5     |
| ◓ | 1.0            | 90.00         | 839.   | 99.41       | -247.4     |

a) Baseline configuration with nacelles.



|   | $\alpha$ , deg | Rn (millions) | q, psf | $P_T$ , psi | $T_T$ , °F |
|---|----------------|---------------|--------|-------------|------------|
| ○ | 1.0            | 8.52          | 318.   | 37.11       | 120.4      |
| □ | 1.0            | 10.23         | 383.   | 44.53       | 120.3      |
| ◇ | 1.0            | 21.51         | 267.   | 31.33       | -201.1     |
| △ | 1.0            | 21.60         | 427.   | 50.01       | -100.2     |
| ▽ | 1.0            | 21.59         | 588.   | 68.71       | -3.991     |
| ◊ | 1.0            | 21.55         | 806.   | 93.82       | 120.5      |
| ◐ | 1.0            | 29.92         | 818.   | 95.31       | -3.984     |
| ◑ | 1.0            | 40.04         | 828.   | 96.39       | -90.18     |
| ◒ | 1.0            | 49.91         | 834.   | 97.22       | -143.1     |
| ◓ | 1.0            | 89.95         | 842.   | 99.40       | -247.1     |

b) Take-off configuration with nacelles.

Figure 12. Longitudinal coefficient trends with Reynolds number, near minimum drag,  $M = 0.30$ .

Figure 12. Concluded.

and that fully turbulent flow existed on both upper and lower surfaces of the inboard wing. Several theoretical curves are included where the variable is the extent of laminar flow on the outboard wing. All theoretical data was adjusted by a constant increment such that the fully turbulent theoretical curve was anchored to the experimental data for the 90 million Reynolds number conditions. The theoretical curves indicate the sensitivity of drag to the transition location on the outboard wing.

The fully turbulent theoretical skin friction drag trend aligned well with the experimental drag data obtained for 21.6 and 30 million Reynolds numbers for the baseline configuration. The drag behavior at this angle of attack suggests that the changes are due primarily to skin friction. The extent of laminar flow inferred from figure 12 compares favorably with temperature sensitive paint measurements of the transition location on the outboard wing for the baseline configuration. The character of the drag for the take-off configuration with changing Reynolds number similarly suggests that skin friction drag reduction is the dominant flow phenomenon. However, there were two distinct groupings of the take-off drag data. One of the groups of data includes Reynolds numbers of 30 million and below (except for the anomalous 430 psf data at  $R_n = 21.6$  million). The second grouping contained all the higher Reynolds number data and the 430 psf data at  $R_n = 21.6$  million. Note also that the higher Reynolds number group closely follows the fully turbulent theoretical skin friction trend.

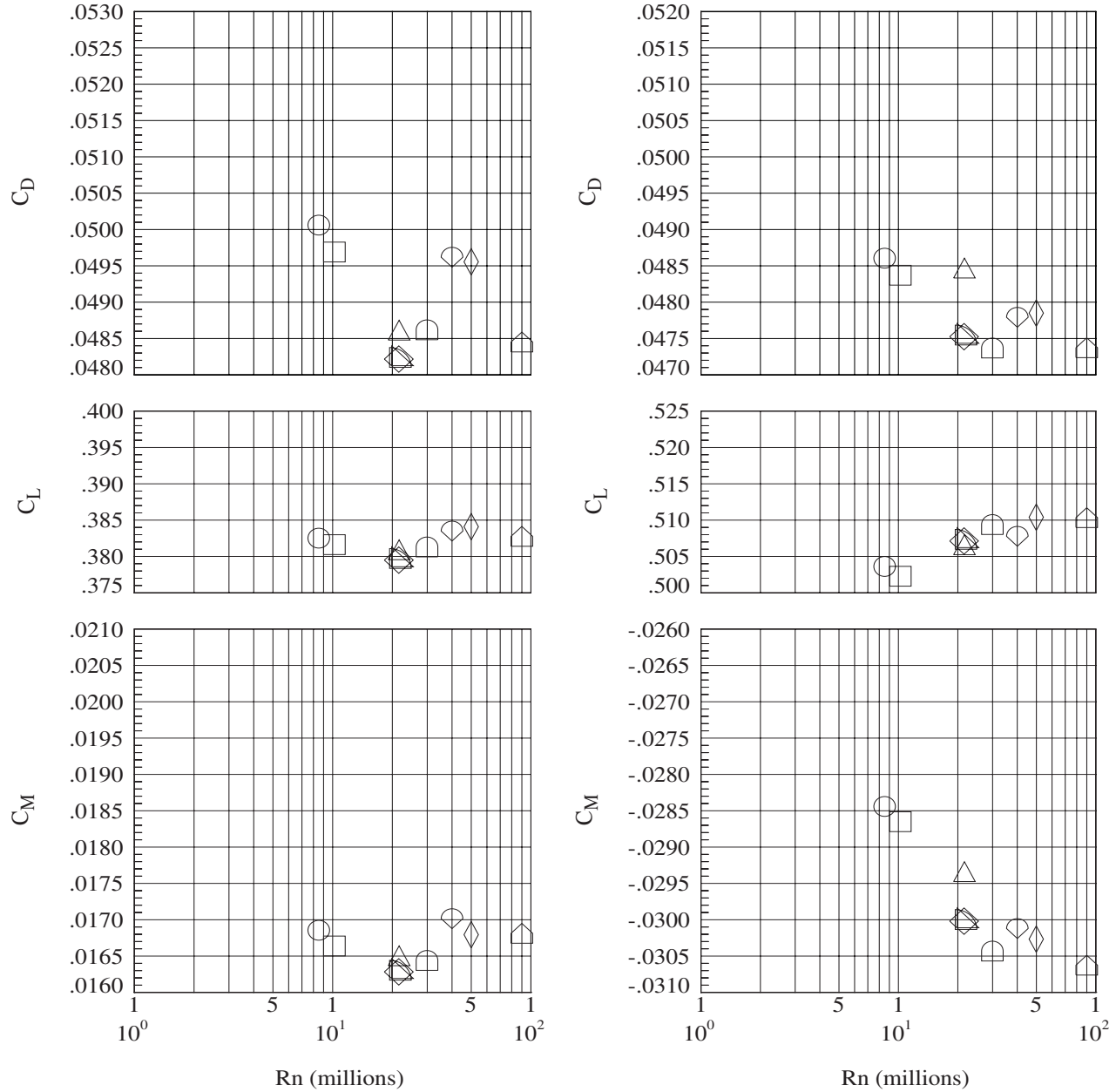
The lift trend with Reynolds number presented in figure 12 for the baseline configuration shows that the lift is essentially constant over the range of Reynolds numbers tested at this angle of attack. The lift for the take-off configuration increases slightly over the range of Reynolds numbers tested. The two distinct data groupings are not apparent in the lift data at this angle of attack.

The pitching moment trends with Reynolds number are presented in figure 12. For reference, the pitching-moment coefficients can be related to the effects of stabilizer deflection. The stabilizer effectiveness for the full configuration with empennage (when closed aftbody and horizontal tails are present) is approximately 0.005 change in pitching-moment coefficient for one degree of stabilizer deflection; one major division represents roughly 0.10 deg of stabilizer to regain trim. For the baseline configuration, the data is essentially

constant. For the take-off configuration, the Reynolds number effect is on the order a 0.4 deg stabilizer change to balance the nose-down pitching moment that develops with the Reynolds number increase. As with lift, the two distinct data groupings were not apparent in the pitching moment data at this angle of attack.

The Reynolds number effects for conditions near the take-off design condition are shown in figure 13. In general, the coefficient trends exhibit the same behavior as that observed at the minimum drag condition. However, the two distinct groups noted in the take-off configuration drag data only (fig. 12) now appear in both the drag and pitching moment data for each configuration.

Since the force and moment data for both configurations show a fundamental shift in drag and pitching moment levels above Reynolds numbers of about 30 million, wing pressures were examined to determine if there was any consistency in this pattern. It is important to note that the pressure data was obtained early in the test and then the pressure tubing was removed to conduct the force and moment testing at the same test conditions. However, the different behavior for the data taken at Reynolds numbers greater than 30 million was consistent between both the pressure and force/moment testing. Typical pressures at or near the wing leading edge as a function of angle of attack are shown in figure 14 for each configuration. In general, the inboard pressures ( $\eta = 0.405$ ) were more sensitive to Reynolds number changes than the pressures on the outboard wing panel ( $\eta = 0.619$ ). The insensitivity of the outboard wing pressures to Reynolds number is due to the sharp, outboard wing leading-edge radius. For the blunt inboard wing pressures, a distinct grouping of the data exists. For each configuration, the data for Reynolds numbers 30 million and below show that the leading-edge flow stays attached to greater angles of attack than for higher Reynolds numbers. There was one exception to this observed trend for each configuration. For the baseline configuration, the leading edge pressure data indicated separation at a lower angle of attack for a Reynolds number of 21.6 million and a dynamic pressure of 426 psf, as discussed previously (see Static Aeroelastic Effects). For the take-off configuration, the different behavior also occurs at a Reynolds number of 21.6 million, but at a dynamic pressure of 268 psf. However, the



|   | $\alpha$ , deg | Rn (millions) | q, psf | $P_T$ , psi | $T_T$ , °F |
|---|----------------|---------------|--------|-------------|------------|
| ○ | 9.0            | 8.51          | 318.   | 37.12       | 120.6      |
| □ | 9.0            | 10.20         | 381.   | 44.52       | 120.3      |
| ◇ | 9.0            | 21.55         | 267.   | 31.32       | -201.5     |
| △ | 9.0            | 21.64         | 430.   | 50.01       | -99.75     |
| ▽ | 9.0            | 21.58         | 587.   | 68.69       | -4.106     |
| ◐ | 9.0            | 21.51         | 803.   | 93.80       | 120.5      |
| ◑ | 9.0            | 29.91         | 817.   | 95.30       | -4.090     |
| ◒ | 9.0            | 40.00         | 825.   | 96.41       | -90.38     |
| ◓ | 9.0            | 49.97         | 834.   | 97.20       | -143.5     |
| ◔ | 9.0            | 90.00         | 839.   | 99.41       | -247.4     |

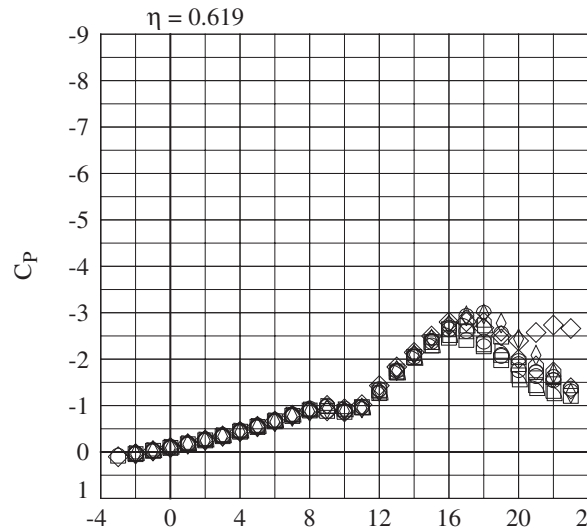
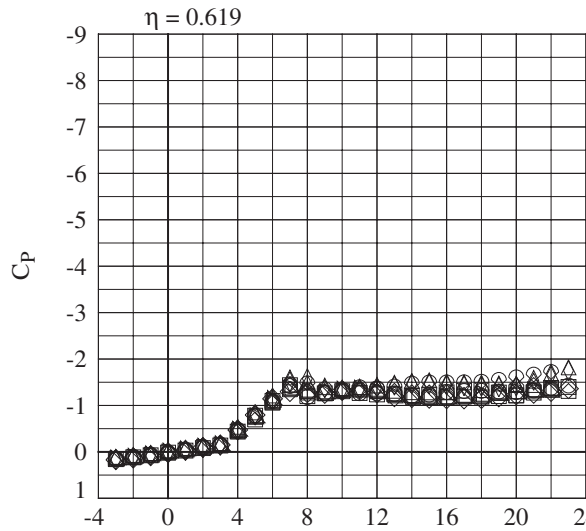
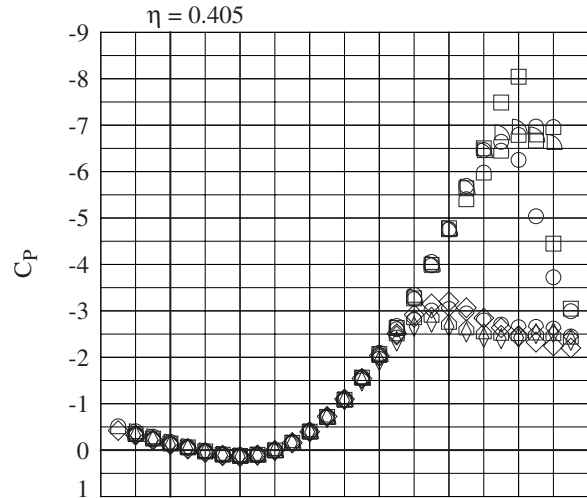
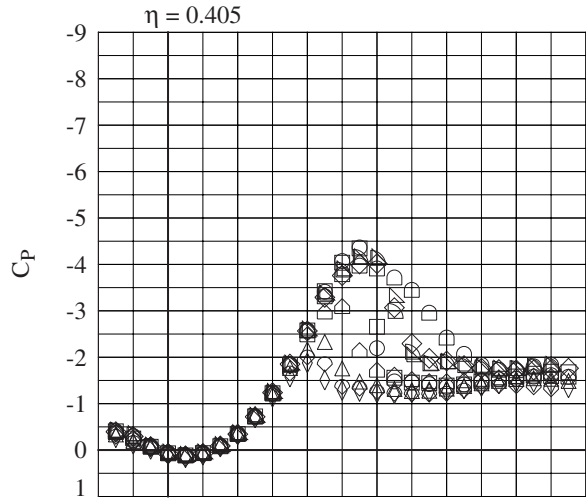
a) Baseline configuration with nacelles.

|   | $\alpha$ , deg | Rn (millions) | q, psf | $P_T$ , psi | $T_T$ , °F |
|---|----------------|---------------|--------|-------------|------------|
| ○ | 9.0            | 8.52          | 318.   | 37.11       | 120.4      |
| □ | 9.0            | 10.23         | 383.   | 44.53       | 120.3      |
| ◇ | 9.0            | 21.51         | 267.   | 31.33       | -201.1     |
| △ | 9.0            | 21.60         | 427.   | 50.01       | -100.2     |
| ▽ | 9.0            | 21.59         | 588.   | 68.71       | -3.991     |
| ◐ | 9.0            | 21.55         | 806.   | 93.82       | 120.5      |
| ◑ | 9.0            | 29.92         | 818.   | 95.31       | -3.984     |
| ◒ | 9.0            | 40.04         | 828.   | 96.39       | -90.18     |
| ◓ | 9.0            | 49.91         | 834.   | 97.22       | -143.1     |
| ◔ | 9.0            | 89.95         | 842.   | 99.40       | -247.1     |

b) Take-off configuration with nacelles.

Figure 13. Longitudinal coefficient trends with Reynolds number, near take-off design point,  $M = 0.30$ .

Figure 13 . Concluded.



|   | Rn (millions) | q, psf | T <sub>T</sub> , °F |
|---|---------------|--------|---------------------|
| ○ | 8.53          | 319.   | 120.1               |
| □ | 10.24         | 383.   | 119.7               |
| ◇ | 21.62         | 267.   | -201.9              |
| △ | 21.59         | 426.   | -100.1              |
| ▴ | 21.59         | 588.   | -4.028              |
| ▷ | 21.55         | 804.   | 120.0               |
| ◊ | 29.91         | 818.   | -3.919              |
| ◇ | 40.06         | 827.   | -90.42              |
| ◇ | 49.93         | 834.   | -143.3              |
| ▷ | 89.94         | 838.   | -247.4              |

a) Baseline configuration with nacelles.

|   | Rn (millions) | q, psf | T <sub>T</sub> , °F |
|---|---------------|--------|---------------------|
| ○ | 8.50          | 317.   | 120.3               |
| □ | 10.20         | 381.   | 120.4               |
| ◇ | 21.57         | 268.   | -201.5              |
| ▷ | 21.52         | 803.   | 119.8               |
| ▷ | 29.92         | 818.   | -4.010              |
| ◇ | 39.92         | 825.   | -89.96              |
| ◇ | 49.94         | 835.   | -143.3              |
| ▷ | 90.00         | 841.   | -247.2              |

b) Take-off configuration with nacelles.

Figure 14. Wing leading-edge pressure characteristics, M = 0.30.

Figure 14. Concluded.

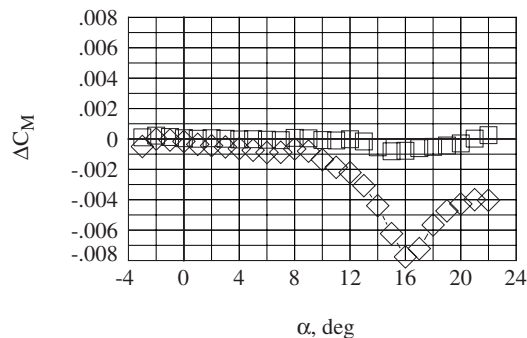
force and moment data used to define the static aeroelastic adjustments for the take-off configuration were acquired separately during the test, and did not show signs of early leading-edge separation.

Both force and moment, and pressure data indicate the wing leading edge separates earlier for Reynolds numbers greater than 30 million, as compared to the lower Reynolds number data. This produced two Reynolds number data groupings in both the drag and pitching moment trends. Note that similar drag and pitching moment trends with increasing Reynolds number exist for both the low and high Reynolds number groups, suggesting the possibility of a flow-state change between the low and high Reynolds number groups that did not significantly change the Reynolds number sensitivity.

To further illustrate the differences in leading-edge separation for the low and high Reynolds number groups, figures 15 and 16 show pitching moment coefficient increments highlighting the effect of Reynolds number. In figure 15, the increments are referenced to the lowest Reynolds number condition, 8.5 million, at the low dynamic pressure level. Increasing the Reynolds number from 8.5 to 21.6 million produces the expected change in pitching moment, especially at the higher angles of attack. In figure 16, the increments are referenced to the

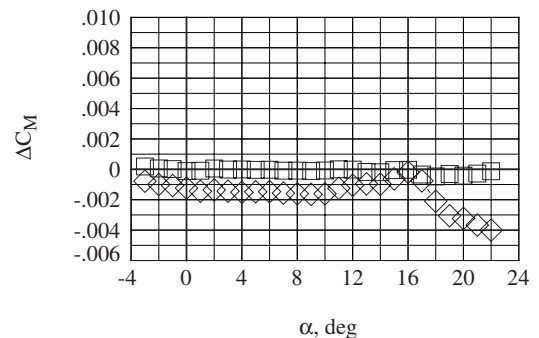
lowest Reynolds number condition, 21.6 million, at the highest dynamic pressure level. The increased nose-up pitching moment relative to the data for Reynolds numbers 30 million and below is clearly seen for both configurations at the higher angles of attack. Also note that within the incremental data for Reynolds numbers greater than 30 million, the nose-up pitching moment increment decreases slightly as the Reynolds number increases. This is consistent with the previously discussed similarity of the Reynolds number trend between the low and high Reynolds number groupings.

Although the cause for the earlier wing leading-edge separation for the higher Reynolds number data is not understood, the Reynolds number effects for both the low and high Reynolds number data groupings appear to be consistent. As Reynolds number increases within each grouping, the drag decrease is consistent with theoretical skin friction reductions. Also, a Reynolds number increase tends to produce a more nose-down pitching moment that is usually associated with a delay in the wing leading-edge separation.



|   | Rn (millions) | P <sub>T</sub> , psi | T <sub>T</sub> , °F | q, psf |
|---|---------------|----------------------|---------------------|--------|
| □ | 10.20         | 44.52                | 120.3               | 381.   |
| ◇ | 21.55         | 31.32                | -201.5              | 267.   |

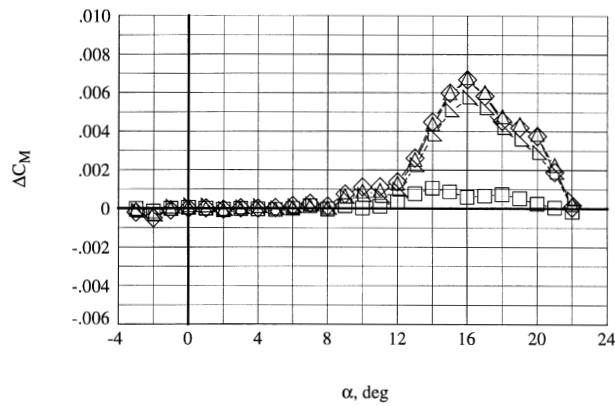
a) Baseline configuration with nacelles.



|   | Rn (millions) | P <sub>T</sub> , psi | T <sub>T</sub> , °F | q, psf |
|---|---------------|----------------------|---------------------|--------|
| □ | 10.23         | 44.53                | 120.3               | 383.   |
| ◇ | 21.51         | 31.33                | -201.1              | 267.   |

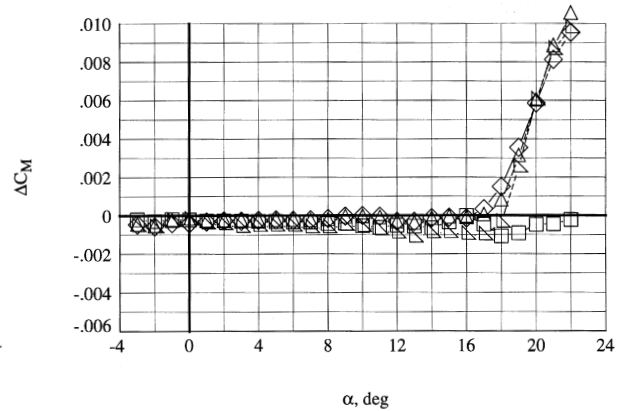
b) Take-off configuration with nacelles.

Figure 15. Pitch-up delay with Reynolds number at low dynamic pressure, M = 0.30.



|   | Rn (millions) | P <sub>T</sub> , psi | T <sub>T</sub> , °F | q, psf |
|---|---------------|----------------------|---------------------|--------|
| □ | 29.91         | 95.30                | -4.090              | 817.   |
| ◇ | 40.00         | 96.41                | -90.38              | 825.   |
| △ | 49.97         | 97.20                | -143.5              | 834.   |
| ▽ | 90.00         | 99.41                | -247.4              | 839.   |

a) Baseline configuration with nacelles.



|   | Rn (millions) | P <sub>T</sub> , psi | T <sub>T</sub> , °F | q, psf |
|---|---------------|----------------------|---------------------|--------|
| □ | 29.92         | 95.31                | -3.984              | 818.   |
| ◇ | 40.04         | 96.39                | -90.18              | 828.   |
| △ | 49.91         | 97.22                | -143.1              | 834.   |
| ▽ | 89.95         | 99.40                | -247.1              | 842.   |

b) Take-off configuration with nacelles.

Figure 16. Pitch-up delay with Reynolds number at high dynamic pressure, M = 0.30.

**CONCLUDING REMARKS**

A series of wind tunnel tests with a 2.2% scale HSCT model was executed in the NTF at NASA LaRC across a wide range of Reynolds numbers from that available in conventional wind tunnels to near flight condition at subsonic and transonic Mach numbers. Results were presented which focus on both the Reynolds number and static aeroelastic sensitivities of longitudinal characteristics at Mach 0.30 for the configuration without the empennage. General conclusions are summarized as follows:

1. Static aeroelastic effects were significant. Increasing the dynamic pressure at constant Mach and Reynolds numbers increases the washout of the outboard wing, which in turn contributes to changes in longitudinal coefficients. Adjustments for static aeroelastic effects can be determined and applied to enable investigation of pure Reynolds number effects.
2. A fundamental change in flow-state occurred between Reynolds numbers of 30 to 40 million, which is characterized by significantly earlier inboard leading-edge separation at the high Reynolds numbers. Force and moment levels change but Reynolds number trends are consistent between the two states. Further studies are necessary to understand the

cause for the changes between Reynolds numbers of 30 and 40 million.

3. Reynolds numbers effects are larger when separated flow dominates at angles of attack above take-off conditions. Separation on the blunt inboard leading edge in particular is sensitive, and significantly impacts the pitching moment characteristics.

**ACKNOWLEDGEMENTS**

The authors would like to thank our many partners from industry and the staff of the NTF for making these tests successful. In particular, we would like to acknowledge Chet Nelson (Boeing), Marvin Hamner (Boeing/McDonnell Douglas), and Susan Williams (NASA-retired) who invested considerable effort over many years towards the development and testing of this model.

**REFERENCES**

1. McKinney, L.W. and Baals, D.D. (editors): "Wind-Tunnel/Flight Correlation – 1981," NASA CP 2225, November 1981.
2. Haines, A.B.: "Scale Effects on Aircraft and Weapon Aerodynamics," AGARD AG-323, 1994.
3. Goldhammer, M.E. and Steinle, F.W. Jr.: "Design and Validation of Advanced Transonic Wings Using CFD and Very High Reynolds

- Number Wind Tunnel Testing,” 17<sup>th</sup> ICAS Congress, September 1990.
4. Lynch, F.T.: “Experimental Necessities for Subsonic Transport Configuration Development,” AIAA Paper 92-0158, January 1992.
  5. Bushnell, D.M., Yip, L.P., Yao, C.S., Lin, J.C., Lawing, P.L., Batina, J.T., Hardin, J.C., Horvath, T.J., Fenbert, J.W., and Domack, C.S.: “Reynolds Number Influences in Aeronautics,” NASA TM 107730, May 1993.
  6. Wilhite, A. W., and Shaw, R. J.: “An Overview of NASA’s High-Speed Research Program,” 20<sup>th</sup> ICAS Congress, Paper 112, August 2000.
  7. Nelson, C.P.: “Effects of Wing Planform on HSCT Off-Design Aerodynamics,” AIAA Paper 92-2629, June 1992.
  8. Wahls, R.A., Owens, L.R., and Rivers, S.M.B.: “Reynolds Number Effects on a Supersonic Transport at Transonic Conditions,” AIAA Paper 2001-0912, January 2001.
  9. Gloss, B. B.: “Current Status and Some Future Test Directions for the US National Transonic Facility,” *Wind Tunnels and Wind Tunnel Test Techniques*, R. Aeronaut. Soc., 1992, pp. 3.1-3.7.
  10. Igoe, W.B.: “Analysis of Fluctuating Static Pressure Measurements in the National Transonic Facility,” NASA TP-3475, March 1996.
  11. Bobbitt, C.W., Hemsch, M.J., and Everhart, J.L.: “NTF Characterization Status,” AIAA Paper 2001-755, January 2001.
  12. Fuller, D.E.: “Guide for Users of the National Transonic Facility,” NASA TM-83124, 1981.
  13. Finley, T.D. and Tcheng, P.: “Model Attitude Measurements at NASA Langley Research Center,” AIAA Paper 92-0763, 1992.
  14. Burner, A.W., Erickson, G.E., Goodman, W.L., and Fleming, G.A.: “HSR Model Deformation Measurements from Subsonic to Supersonic Speeds,” 1998 NASA High-Speed Research Program Aerodynamic Performance Workshop, February 1998, NASA/CP-1999-209692, Vol. 1, p. 1569-1588.
  15. Foster, J.M. and Adcock, J.B.: “User’s Guide for the National Transonic Facility Research Data System,” NASA TM-110242, April 1996.
  16. Williams, M.S.: “Experience with Strain Gage Balances for Cryogenic Wind Tunnels,” AGARD-R-774, 1989, pp. 18.1-18.14.
  17. Braslow, A.L., and Knox, E.C.: “Simplified Method for Determination of Critical Height of Distributed Roughness Particles for Boundary-Layer Transition at Mach Numbers from 0 to 5,” NACA TN-4363, 1958.
  18. Wahls, R.A., Adcock, J.B., Witkowski, D.P., and Wright, F.L.: “A Longitudinal Aerodynamic Data Repeatability Study for a Commercial Transport Model in the National Transonic Facility,” NASA TP-3522, August 1995.
  19. Wahls, R.A., Gloss, B.B., Flechner, S.G., Johnson, W.G., Jr., Wright, F.L., Nelson, C.P., Nelson, R.S., Elzey, M.B., and Hergert, D.W.: “A High Reynolds Number Investigation of a Commercial Transport Model in the National Transonic Facility,” NASA TM-4418, April 1993.
  20. Al-Saadi, J.A.: “Effect of Reynolds Number, Boundary-Layer Transition, and Aeroelasticity on Longitudinal Aerodynamic Characteristics of a Subsonic Transport Wing,” NASA TP-3655, September 1997.
  21. Payne, F.M., Wyatt, G.W., Bogue, D.R., and Stoner, R.C.: “High Reynolds Number Studies of a Boeing 777-200 High Lift Configuration in the NASA ARC 12’ Pressure Tunnel and NASA LaRC National Transonic Facility,” AIAA Paper 2000-4220, August 2000.
  22. Sommer, S.C., and Short, B.J.: “Free-Flight Measurements of Turbulent-Boundary-Layer Skin Friction in the Presence of Severe Aerodynamic Heating at Mach Numbers from 2.8 to 7.0,” NASA TN-3391, March 1955.